

Dual fluorescence-absorption deconvolution applied to extended-depth-of-field microscopy

WILLIAM J. SHAIN,¹ NICHOLAS A. VICKERS,² AWOKE NEGASH,⁴ THOMAS BIFANO,³
ANNE SENTENAC,^{4,*} AND JEROME MERTZ^{3,5}

¹Department of Physics, Boston University, 590 Commonwealth Avenue, Boston, Massachusetts 02215, USA

²Department of Mechanical Engineering, Boston University, 110 Cummington Mall, Boston, Massachusetts 02215, USA

³Photonics Center, Boston University, 8 Saint Mary's St., Boston, Massachusetts 02215, USA

⁴Aix Marseille Université, CNRS, Centrale Marseille, Institut Fresnel, UMR 7249, 13013 Marseille, France

⁵Department of Biomedical Engineering, Boston University, 44 Cummington Mall, Boston, Massachusetts 02215, USA

*Corresponding author: anne.sentenac@fresnel.fr

Received 24 August 2017; revised 21 September 2017; accepted 22 September 2017; posted 22 September 2017 (Doc. ID 301292); published 13 October 2017

Fast imaging over large volumes can be obtained in a simple manner with extended-depth-of-field (EDOF) microscopy. A standard technique of Wiener deconvolution can correct for the blurring inherent in EDOF images. We compare Wiener deconvolution with an alternative, parameter-free technique based on the dual reconstruction of fluorescence and absorption layers in a sample. This alternative technique provides significantly enhanced reconstruction contrast owing to a quadratic positivity constraint that intrinsically favors sparse solutions. We demonstrate the advantages of this technique with mouse neuronal images acquired *in vivo*. © 2017 Optical Society of America

OCIS codes: (100.1830) Deconvolution; (100.3010) Image reconstruction techniques; (180.2520) Fluorescence microscopy.

<https://doi.org/10.1364/OL.42.004183>

There has been a recent push to develop microscopes that provide fast imaging over large fields of view (FOVs). This push has been largely propelled by the neurobiology community, with the aim of monitoring the population dynamics of hundreds, if not thousands, of neurons *in vivo*, spanning areas as large as a few square millimeters [1]. To perform high-speed imaging over such large FOVs poses a challenge. For example, calcium indicators currently have response times on the order of 100 ms [2]. On the other hand, a new generation of voltage indicators whose response times are on the order of only a few milliseconds is becoming available [3,4]. To attain such speeds, microscopes based on point scanning are at a disadvantage, and camera-based microscopes seem to be a better option. However, even with a camera, it is difficult to image over large volumes (as opposed to areas) at a high speed, since this typically requires the acquisition of stacks of multiple images.

A partial solution to this problem is to perform quasi-volumetric, or extended-depth-of-field (EDOF), imaging, where depth resolution is sacrificed in favor of speed. For

example, EDOF imaging can be obtained from fast focal sweeps [5–7] within individual camera exposure times, attaining DOF extensions of a few hundreds of microns.

Recently, we demonstrated fast EDOF imaging with a deformable mirror (DM) that features a 20 kHz update rate [8]. Our same setup is illustrated in Fig. 1, and is basically a standard epi-fluorescence microscope equipped with an additional optical relay between the intermediate image plane and the camera. This relay provides access to a pupil plane where we inserted the DM (MultiDM, Boston Micromachines Corp.). By adjusting the curvature of the DM, positive or negative, we sweep the focus of the microscope over a range D during a single camera exposure, thus obtaining EDOF images (see [8] for details).

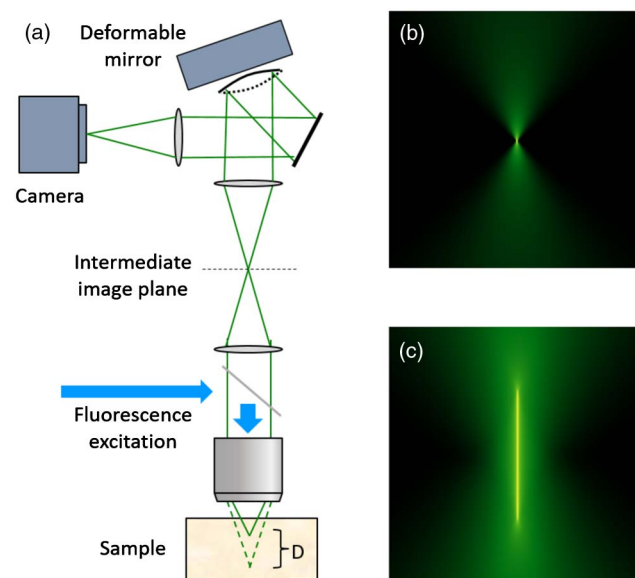


Fig. 1. (a) Schematic of EDOF Microscope. (b) $x-z$ section of standard 3D PSF. (c) $x-z$ section of a 3D EPSF. Logarithmic scale.

However, EDOF images are peculiar. Because all objects within a focal sweep are, at one time during the sweep, in focus, EDOF images may be considered all-in-focus. On the other hand, by the same argument, they may equally be considered all-out-of-focus. Sharp structures in EDOF images are thus systematically surrounded by a blurry haze. More rigorously, a 2D EDOF image is the convolution, restricted to the observation plane, of the 3D extended point spread function (EPSF) and the 3D sample itself. The 3D EPSF can be estimated using the knowledge of the microscope standard PSF and the focal-sweep range [9], as illustrated in Fig. 1. We note that the transverse EPSF is remarkably constant throughout the focal-sweep range, making it possible to approximate the 3D convolution as a 2D convolution acting on the fluorescence distribution integrated over this focal-sweep range. An estimate of this integrated fluorescence distribution σ can then be obtained by solving the minimization problem [10]

$$\arg \min_{\sigma} \|I - \sigma * \text{EPSF}\|^2, \quad (1)$$

where I is the experimentally acquired EDOF image, and EPSF is the representative 2D EPSF. Such a minimization problem can be solved using either direct Wiener deconvolution [8,9] or an iterative gradient descent.

We found that while Wiener deconvolution was very effective when applied to simple samples [8], such as fluorescent beads in agarose, it was somewhat less effective when applied to more relevant samples, such as in-vivo fluorescently labeled neurons in mice brains. A reason for this is that our 2D convolution model neglected all fluorescence contributions from beyond the range of the focal sweep. When imaging in thick tissue, such contributions clearly should not be neglected as they produce a significant amount of light at the camera. The purpose of this Letter is to improve upon our past results and develop a deconvolution strategy specifically designed for thick tissue fluorescence imaging. In addition to addressing the problem of far-out-of-focus diffuse fluorescence, we also make an important allowance for the presence of absorbing structures within the sample. We confirm the validity of our strategy with both simulation and experiment.

A closer examination of the 3D EPSF in the $x-z$ panel depicted in Fig. 1 shows that three distinct layers are apparent, one above, one within, and one below the focal-sweep region. As noted above, for objects located within the focal-sweep layer, the 3D EPSF is quasi-constant, justifying the use of a representative 2D EPSF specifically for this layer. However for objects outside this layer, the function spreads rapidly, producing a highly blurred background. It is this blurred background that was not properly taken into account by our representative 2D EPSF. In practice, this blurred background arises from fluorescent objects located in the bottom layer deep within the sample and beyond the reach of the focal sweep. (We neglect the top layer since the focal sweep is assumed to start from the sample surface.)

The effect of a deep fluorescent layer is two-fold. It produces not only a highly blurred background, but also a back-light that trans-illuminates the focal-sweep layer of interest. With such trans-illumination, we must be careful in how we treat the presence of absorbing objects. Specifically, absorbing objects within the focal-sweep layer no longer appear simply as an absence of fluorescence, but rather as a presence of *negative* fluorescence, in the sense that they remove fluorescence from the back-light.

In the simplest model, because of multiple scattering, the signal produced by this back-light may be treated as a uniform constant B over the entire FOV, which we can incorporate into our minimization algorithm

$$\arg \min_{\sigma} \|I - B - \sigma * \text{EPSF}\|^2, \quad (2)$$

where σ here can take on both positive and negative values, corresponding to fluorescent emitters or absorbers, respectively. However, the net effect of this modification to Eq. (1) is minor, since all it does is introduce an offset to the previous minimization solution. In addition, the interpretation of σ as emitters or absorbers critically depends on the estimation of B . (Generally, B is taken equal to $\max(I)$ since the fluorescence in the focal-sweep region is usually much weaker than the background light.) Another more robust means of sample estimation is desirable. In particular, deconvolution strategies that make use of positivity constraints and sparsity assumptions have been shown to provide significantly improved results over standard Wiener deconvolution [11,12], though they usually do not account for absorption.

In this Letter, we adapt a strategy previously used for speckle fluorescence imaging [11] to take into account both fluorescence and absorption. The idea is to separate σ into distinct fluorescence and absorption components, where we make explicit the constraint that fluorescence must be positive and absorption must be negative. With this new technique, our deconvolution strategy becomes a two-component least-squares minimization problem:

$$\arg \min_{\sigma_{\text{flu}}, \sigma_{\text{abs}}} \|I - B - (\sigma_{\text{flu}}^2 - \sigma_{\text{abs}}^2) * \text{EPSF}\|^2. \quad (3)$$

The purpose of squaring the parameters σ_{flu} and σ_{abs} is two-fold. First, it guarantees their positivity [corresponding to a negativity for absorption owing to the sign inversion in Eq. (3)]. Secondly, our iterative minimization algorithm preferentially avoids converging to small values of σ_{flu} or σ_{abs} because it is based on a gradient descent. (Gradients of quadratic parameters become small when the parameters themselves become small.) In other words, the squaring of the search parameters effectively leads to a soft thresholding in their reconstruction, thus helping favor sparse (i.e., more contrasted) solutions [11]. In all the following examples, the initial estimates are taken to be a constant throughout the FOV, and iterative minimization is terminated upon optimized reconstruction as determined by the eye, which has been shown to be equivalent to Tikhonov regularization [10].

We first compare the performances of dual fluorescence absorption (DFA) reconstruction and Wiener deconvolution using simulated data. We numerically generate an en-face EDOF image of fluorescent emitters close to an absorbing band (e.g., mimicking fluorescent neurons close to an absorbing blood vessel). A constant back-light is also introduced to simulate far-out-of-focus fluorescence. Since the emitters and absorbers are in the focal-sweep region, their image is modeled using the EPSF. To simulate typical experimental conditions, we corrupted the image with Poisson noise associated with a maximum of 10^4 photons per pixel (most of which are back-light). The raw image and reconstructions are displayed in Fig. 2. DFA reconstruction manifestly provides more contrast than Wiener deconvolution, while still maintaining a good estimate of the relative strength of the emitters.

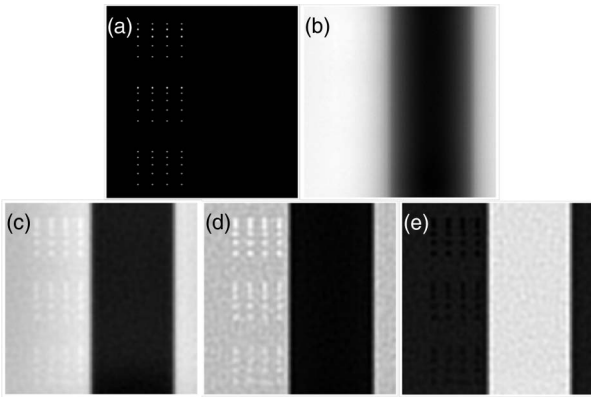


Fig. 2. Simulations of fluorescent emitters that become weaker from top to bottom. (a) Ground-truth fluorescence, (b) raw image, (c) Wiener, (d) fluorescence, and (e) absorption reconstructions using two-layer algorithm of Eq. (2).

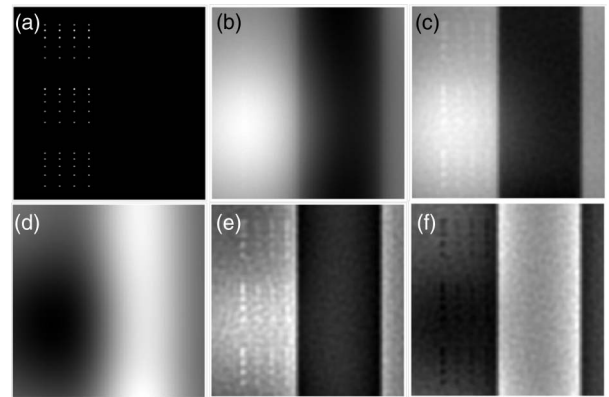


Fig. 3. Simulations of fluorescent emitters of the same strengths. (a) Ground-truth fluorescence, (b) raw image, (c) Wiener, (d) back-light absorption, (e) fluorescence, and (f) absorption reconstructions using three-layer algorithm of Eq. (3).

The model used in Eq. (3), nevertheless, remains overly simplistic as the fluorescence back-light B is constant over the entire FOV. To take into account the possibility of spatial variations in B , we replace our two-layer model with a three-layer model. In this more realistic model, the top layer is the focal-sweep layer or interest, the bottom is a layer so deep that the back-light B produced by it may be safely taken to be a constant. Between these, we introduce an intermediate layer in which we allow the presence of additional absorbers, of distribution denoted by η_{abs}^2 . Because these absorbers are situated in a layer beyond the range of the focal sweep, the PSF associated with their imaging is quite blurred, so blurred that it can be approximated by a phenomenological 2D Gaussian, denoted by GPSF. The width of this Gaussian can be chosen depending on the sample being imaged, and should be roughly commensurate with the range of long-scale variations apparent in the back-light intensity of the experimentally acquired EDOF images. In short, the back-light intensity in this three-layer model is modulated by the blurred intermediate absorbing structures. To take this modulation into account, our deconvolution strategy becomes a three-parameter minimization problem:

$$\arg \min_{\eta_{\text{abs}}, \sigma_{\text{fluo}}, \sigma_{\text{abs}}} \|I - B + \eta_{\text{abs}}^2 * \text{GPSF} - (\sigma_{\text{fluo}}^2 - \sigma_{\text{abs}}^2) * \text{EPSF}\|^2. \quad (4)$$

Again, the key parameter of interest is generally σ_{fluo}^2 . The other parameters are collateral, and may or may not be of interest. Simulation results with this new model are shown in Fig. 3. Despite the deleterious effects of non-uniform back-light, both deconvolution strategies are able to reveal fluorescence emitters that are difficult to discern otherwise, with DFA continuing to outperform Wiener deconvolution in terms of reconstruction contrast.

We now turn to experimental results. Figure 4 demonstrates the application of Wiener and three-layer DFA deconvolution to in-vivo mouse brain imaging of GCaMP-labeled cortical neurons. EDOF microscopy was performed with an air-immersion objective (Olympus 10 \times , NA = 0.3) and a camera exposure time of 100 ms (PCO Edge). The EDOF range was about 200 μm . The raw image [Fig. 4(a)] shows only a hazy structure of low contrast, where large blood vessels are visible, while

fluorescent neurons are just barely distinguishable from the background. Wiener deconvolution provides substantial contrast improvement, where the neurons not only become more discernible, but also the finer capillaries become better delineated. Such contrast improvement is similar to the results reported in Ref. [8], as expected since the Wiener deconvolution strategy is essentially the same.

Much more significant is the contrast improvement obtained with DFA deconvolution, where the fluorescence and absorption distributions are separately reconstructed. Perhaps a better illustration of this contrast improvement comes from a projection of the image frames in time (Fig. 5). Neuronal

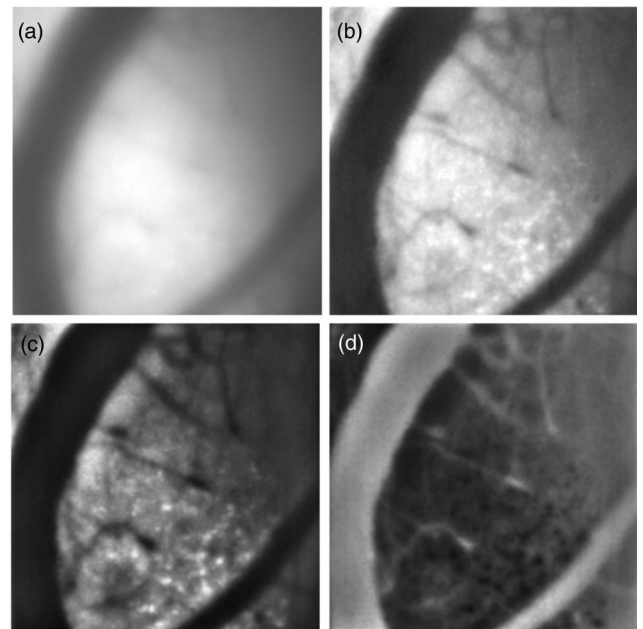


Fig. 4. Time series of (a) raw image, (b) Wiener, (c) fluorescence, and (d) absorption reconstructions of GCaMP-labeled neurons in mouse cortex. (a)–(c) Maximum intensity projections and (d) a minimum intensity projection. FOV \approx 250 μm .

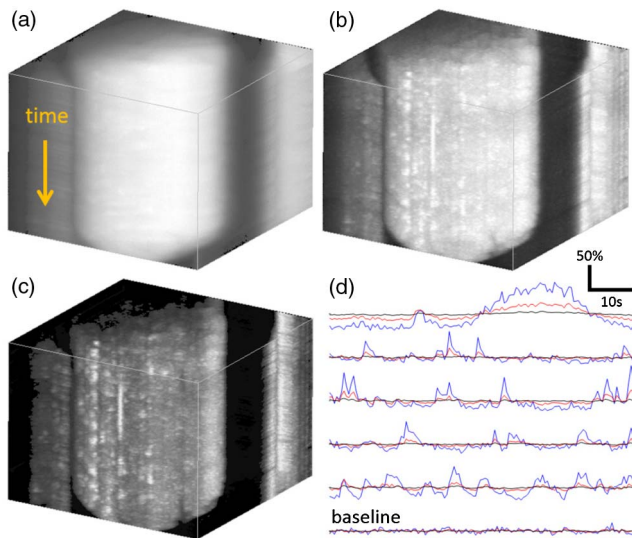


Fig. 5. Time series of (a) raw image (black), and (b) Wiener (red) and (c) DFA reconstructions (blue) from Fig. 4. (d) Plots of the time courses of selected neuronal signals, normalized to their respective means. Vertical scale = $\Delta F/F$.

activity is essentially invisible in the raw images, whereas it becomes visible with Wiener deconvolution and quite striking with DFA deconvolution.

Our example of imaging mouse neuronal activity *in vivo* was not chosen at random. Indeed, such imaging is of considerable utility in the neuroscience community, where the identification of where and when neurons become active provides key information about their dynamics. In Fig. 5(d), we provide plots of the activity of selected cells within the EDOF volume, along with a baseline for a comparison of noise levels. Again, we see that neuronal activity only becomes apparent upon deconvolution, and that this activity is significantly magnified upon DFA deconvolution. A question remains as to how quantitative this magnification is. For example, Wiener deconvolution, as defined by Eqs. (1) or (2), is manifestly linear. DFA deconvolution, on the other hand, does not appear at first glance to be linear. Nevertheless, a scatter plot derived from Fig. 6 comparing the fluorescence levels obtained with both deconvolution methods reveals that, despite its appearance, DFA deconvolution seems to preserve a high degree of linearity.

In summary, we have demonstrated that both Wiener and DFA deconvolution are very helpful in extracting features of interest from otherwise largely featureless EDOF images. Both techniques have advantages and disadvantages. The main advantage of Wiener deconvolution is speed, since it does not require iterative minimization, but can be obtained directly by division in Fourier space (e.g., [8,9]). The main advantage of DFA deconvolution is significantly increased reconstruction contrast, at the cost, however, of speed. (Our reconstructions took about 20 s per image running on a standard desktop computer.) Another potential disadvantage is failure to converge to the proper minimum since the cost function in Eq. (3) is only locally convex (though we observed no such failure in our trials). The question of which technique to adopt thus depends on the application. In either case, deconvolution provides clear

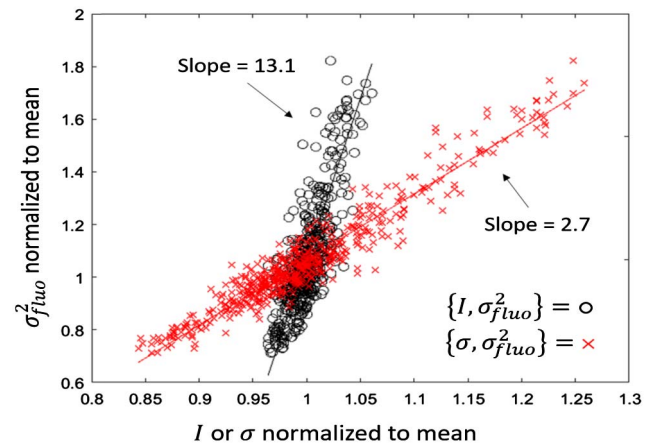


Fig. 6. Scatter plots and linear regressions of σ_{fluor}^2 versus I (black o) and σ_{fluor}^2 versus σ (red x) based on data in Fig. 5(d). Plots indicate that DFA reconstruction appears to be linear, with the contrast improved by a factor of about 3 compared to Wiener deconvolution, and 13 compared to the raw image.

benefits to EDOF imaging, which may be useful, for example, in monitoring neuronal dynamics over large scales.

Funding. National Eye Institute (NEI) (R21EY026310); National Science Foundation (NSF) (IIP-1068070); Fulbright Fellowship.

Acknowledgment. The authors acknowledge the support of the National Science Foundation Industry/University Cooperative Research Center for Biophotonic Sensors and Systems and the National Institute of Health. They also thank the X. Han lab and specifically A. I. Mohammed for providing mice. A. Sentenac is partially funded by a Fulbright fellowship. T. Bifano acknowledges a financial interest in Boston Micromachines Corporation.

REFERENCES

- N. Ji, J. Freeman, and S. L. Smith, *Nat. Neurosci.* **19**, 1154 (2016).
- A. Badura, X. R. Sun, A. Giovannucci, L. A. Lynch, and S. S.-H. Wang, *Neurophotonics* **1**, 025008 (2014).
- Y. Gong, C. Huang, J. Z. Li, B. F. Grewe, Y. Zhang, S. Eismann, and M. J. Schnitzer, *Science* **350**, 1361 (2015).
- A. S. Abdelfattah, S. L. Farhi, Y. Zhao, D. Brinks, P. Zou, A. Ruangkittisakul, J. Platasa, V. A. Pieribone, K. Ballanyi, A. E. Cohen, and R. E. Campbell, *J. Neurosci.* **36**, 2458 (2016).
- E. Botcherby, R. Juskaitis, M. Booth, and T. Wilson, *Opt. Lett.* **32**, 2007 (2007).
- M. Duocastella, B. Sun, and C. B. Arnold, *J. Biomed. Opt.* **17**, 050505 (2012).
- C. C. Archer-Zhang, W. B. Foster, R. D. Downey, C. L. Arrasmith, and D. L. Dickensheets, *J. Biomed. Opt.* **21**, 121507 (2016).
- W. Shain, N. A. Vickers, B. B. Goldberg, T. Bifano, and J. Mertz, *Opt. Lett.* **42**, 995 (2017).
- S.-H. Lu and H. Hua, *Opt. Express* **23**, 10714 (2015).
- M. Bertero and P. Boccacci, *Introduction to Inverse Problems in Imaging* (CRC Press, 1998).
- A. Negash, S. Labouesse, N. Sandeau, M. Allain, H. Giovannini, J. Idier, R. Heintzmann, P. C. Chaumet, K. Belkebir, and A. Sentenac, *J. Opt. Soc. Am. A* **33**, 1089 (2016).
- S. Labouesse, A. Negash, and J. Idier, *IEEE Trans. Image Process.* **26**, 2480 (2017).